Intermittent transport events in a cylindrical plasma device: Experiment and Simulation

T. Windisch[1], O. Grulke[1,2], V. Naulin[3], T. Klinger[1,2]

[1] Max-Planck-Institute for Plasma Physics, EURATOM Association, D-17491 Greifswald, Germany
[2] Ernst-Moritz-Arndt University, D-17489 Greifswald, Germany
[3] Risø DTU, Technical University of Denmark

E-mail: thomas.windisch@ipp.mpg.de

Abstract. The origin of intermittent fluctuations in the plasma edge of a linearly magnetized plasma column is investigated and closely compared to three-dimensional global numerical simulations. The intermittent character is caused by radially propagating turbulent structures. The radial propagation of the structures is due to the self-consistent potential perturbation associated with them. Their formation is closely linked to transport events caused by nonlinear drift-wave fluctuations. In the formation region a sheared azimuthal flow velocity is observed, which is driven by the Reynolds stress.

PACS numbers: 52.35.Kt,52.35.Ra,52.35.Mw

Keywords: intermittency, turbulence, drift-waves, transport, coherent structures

1. Introduction

Intermittent fluctuations can roughly be described as the occurrence of sporadic large-amplitude bursts within a quiescent background, which leads to strong deviations from Gaussian statistics [1]. This can be observed in a variety of physical systems, e.g. in turbulent hydrodynamic flows [2], magnetohydrodynamic turbulence in geophysics [3], in the solar wind [4, 5], and in plasma turbulence [6, 7]. It is known since decades that intermittency in hydrodynamic turbulence is linked to the formation of turbulent coherent structures (vortices) [8]. Intermittent fluctuations are of special interest because they lead to deviations from self-similarity, which is a basic assumption of turbulent energy cascades [9]. Intermittency thus alters the observed scaling laws [10]. In contrast to three-dimensional turbulence, vortex stretching does not occur in two-dimensional plasma turbulence. The consequential conservation of vorticity is the root for the socalled dual cascade [11]. While energy is mainly transferred to the largest spatial scales in the system, enstrophy is transferred to the smallest spatial scales. Vortices can merge and the energy may finally condense in large-scale coherent structures or large-scale shear flows (zonal flows) [12]. In plasma turbulence, zonal flows can be driven by the nonlinear energy transfer from drift waves mediated through the wave-induced Reynolds stress [13]. As energy is transferred from drift-wave turbulence to the zonal flow, the turbulent energy and consequently the related transport is reduced. In the absence of such turbulence reduction the convective particle flux across the confining magnetic field of fusion devices is governed by intermittent transport events, which are related to radially propagating large-scale coherent structures [14, 15]. Due to their quasi two-dimensional localization ($k_{\|} \approx 0$) they are often termed 'filaments' [16]. The turbulent structures develop in the shear layer associated with the transition from closed and open magnetic flux surfaces [17] and propagate radially outwards across the entire scrape-off layer (SOL) region towards the wall.

The typical radial structure velocity is of the order of 10% of the local ion sound speed [15]. The radial propagation of the structures in the region of open magnetic flux surfaces has been identified to be due to the interchange mechanism, which is based on the curvature of the magnetic field [18]. Details of the formation of these turbulent structures in the plasma edge still need clarifications, but experimental data for fusion devices, especially spatiotemporal resolved data, are hard to obtain due to limitations in the available diagnostics. Numerical simulations suggest, however, that drift-wave turbulence plays a crucial role in the plasma edge region [19]. Although the radial propagation of turbulent structures in the SOL of fusion devices is caused by the magnetic field curvature, radially propagating turbulent structures are also observed in laboratory devices with straight magnetic field geometry [20, 21]. The interchange drive is absent and thought to be replaced by centrifugal or neutral wind forces [22].

In this paper the spatiotemporal dynamics of turbulent structures is investigated in the cylindrical magnetized plasma column of the laboratory device VINETA [23]. Special attention is paid to (a) the radial propagation mechanism of the structures in the plasma edge and (b) to the structure formation mechanism, which is directly related to the primary drift-wave instability. The structure formation occurs in a region, in which the phase velocity of the fluctuation is subject to a strong shear. The origin of this shear layer and its relation to the Reynolds stress are discussed. The experimental findings are compared to three-dimensional global numerical simulations with realistic boundary conditions [24].

The paper is organized as follows: In Sec. 2 the experimental setup and basic characteristics of the numerical simulation are presented. In Secs. 3 and 4 the intermittent character of the fluctuations and the link to spatiotemporal turbulent structures are analyzed. The formation process of these turbulent structures is discussed in Sec. 5. Finally, in Sec. 6, the results are summarized and discussed.

2. Setup and basic characteristics of experiment and numerical simulation

2.1. Experiment

The experiments were done in the linearly magnetized helicon device VINETA [23]. A schematic diagram is shown in Fig.1. It consists of a grounded stainless steel vacuum chamber (diameter $d = 40\,\mathrm{cm}$, length $L_{\parallel} = 4.5\,\mathrm{m}$), with 36 magnetic field coils that provide a homogeneous straight magnetic field up to $B = 100\,\mathrm{mT}$. Plasma is produced using a conventional helicon source [25] with a right-handed helical antenna ($m = +1$) placed around a glass vacuum extension ($d = 10\,\mathrm{cm}$), which determines the typical plasma radius $r_p \approx 5\,\mathrm{cm}$. The antenna is coupled to a radio-frequency (RF) source ($\omega_{\mathrm{RF}}/2\pi = 13.56\,\mathrm{MHz}$, $P_{\mathrm{RF}} \leq 5\,\mathrm{kW}$) via a capacitive L-matching circuit [26]. All measurements presented here are done with Argon as working gas. The plasma parameters as well as the typical length and time scales are compiled in Tab. 1. As a general feature of helicon discharges, a dense plasma at low electron temperatures is produced, which leads to a fairly high Coulomb collisionality. Time-averaged plasma parameters are measured with Langmuir probes that are compensated against RF fluctuations [27]. The absolute plasma density is cross-calibrated with the line integrated density measured with a 160 GHz interferometer. Fluctuations of the plasma density and potential are measured with uncompensated probes. Plasma density fluctuations are measured in the ion saturation current regime at a probe bias of $U = -100$ V with respect to the grounded plasma vessel. We assume that electron temperature fluctuations are negligible, such that $\tilde{I}_{\mathrm{sat}} \sim \tilde{n}$ holds. Based on the same assumption, the floating potential fluctuations is used as an estimate of plasma potential fluctuations. To gain insight into spatiotemporal fluctuations, multiple Langmuir probes are arranged as probe arrays, e.g., an azimuthal array consisting of 64 probe pins at a fixed radial location [28]. Single probes are mounted on two-dimensional probe positioning systems to move the probe automatically across the entire plasma cross section. The space-time behavior is then reconstructed by applying statistical techniques as cross-correlation or conditional averaging [29, 30]. Magnetic fluctuations are measured with a three-axis miniaturized induction coil ($\dot{B}$-probe) [31]. Fluctuations of the parallel current $\tilde{j}_z$ are determined from Ampere's law.

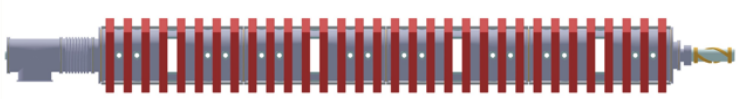

Figure 1. Schematic drawing of the VINETAdevice. For better visualization the magnetic field coils which surround the plasma source have been skipped.

plasma parameter	value	unit
absorbed RF power P_{RF}	2	kW
Argon neutral gas pressure p_0	0.08	Pa
magnetic field B_0	80	mT
plasma density n	6	$10^{18}\,\mathrm{m}^{-3}$
electron temperature T_e	2.5	eV
ion temperature T_i	0.2	eV
drift scale ρ_s	1.8	cm
ion sound speed c_s	2.5	km s−1
electron plasma frequency $\omega_{p,e}$	1.4	$10^{11}\,\mathrm{rad\ s}^{-1}$
ion gyro frequency ω_{ci}	1.9	$10^{5}\,\mathrm{rad\ s}^{-1}$
Coulomb collision frequency ν_{ei}	4.5	$10^{7}\,\mathrm{rad\ s}^{-1}$
Ion-neutral collision frequency ν_{in}	6	$10^{3}\,\mathrm{rad\ s}^{-1}$
Electron neutral collision frequency ν_{en}	6	$10^{5}\,\mathrm{rad\ s}^{-1}$

Table 1. VINETA operational and plasma parameters of the measurements presented here.

2.2. Numerical simulation

To compare the experimental findings with numerical simulation results we use the three-dimensional numerical simulation code CYTO [24], which solves the two-fluid equations in a cylindrical geometry. For a detailed description of the CYTO equations, as wells as its linear properties the reader is referred to Ref. [24]. A specific feature of the CYTO simulation is its global character: Time-averaged and fluctuating quantities are not treated separately, i.e., the Reynolds decomposition $n = n_0 + \tilde{n}$ with $\tilde{n} \ll n_0$ is not applied. This is of special importance in the plasma edge region, in which the amplitude of the intermittent density bursts $\tilde{n}$ may exceed n_0 by almost an order of magnitude and consequently the assumption of a small fluctuation amplitude does not hold. If only fluctuations are considered, the CYTO equations reduce to the well known Hasegawa-Wakatani equations [32], which are commonly used to describe nonlinear drift waves. In the CYTO simulation, a Gaussian density source with a fixed parallel decay length $S = \exp\left(-r^2\kappa_n^2\right)\exp\left(-z^2\right)$ is used. All other parameters evolve fully self-consistent. The parallel density flux $nv_\parallel$ at the end of the device ($z = L_\parallel$) is assumed to have zero parallel derivative while the boundary conditions for the potential and velocity are Bohm sheath boundary conditions.

VINETA parameter	value	CYTO input parameter	value
plasma density n [m^{-3}]	10^{18}	gradient length κ_n [ρ_s]	0.5
electron temperature T_e [eV]	2	electron-ion collision frequency ν [ω_{ci}]	56
ion temperature T_i [eV]	0.2	electron-neutral collision frequency δ [ω_{ci}]	2.7
magnetic field B_0 [mT]	80	ion-neutral collision frequency σ [ω_{ci}]	0.04
Argon gas pressure p_0 [Pa]	0.1	ion viscosity μ [ω_{ci}]	0.001

Table 2. VINETA and derived CYTO input parameters.

The physical input parameters are the normalized collisionalities, viscosity, and the gradient length κ of the Gaussian density profile. They are derived from typical

VINETA parameters to be consistent with the experimental situation presented in Sec. 2.1. They are compiled in Tab. 2. The computational grid is $(40, 64, 32)$ in the (r, θ, z) domain and spans over $12.5\,\rho_s$ in the radial and $125\,\rho_s$ in the parallel direction ($\rho_s = 1.6\,\mathrm{cm}$).

The temporal evolution of the total fluctuation energy $E_{tot} = \int (\tilde{n}\nabla_\perp\tilde{\phi})^2\ d^3r$ is shown in Fig. 2a. It is characterized by an exponential growth in the linear phase ($t \leq 1.5\,\mathrm{ms}$) and subsequent nonlinear saturation in the turbulent state. Two snapshots of the total density and the fluctuating part in the linear and nonlinear saturated state are shown in Fig. 2b-e. Note that, unless otherwise stated, the data has been taken at the axial center of the plasma column. The two time instants are indicated in Fig. 2a as red lines. In the linear phase (Fig. 2b-c) the fluctuation amplitude is small ($\tilde{n}/n \approx 0.03$) and the density profile is determined by the Gaussian source profile. The $m = 3$ drift mode has the largest growth rate. In the nonlinear saturated state (Fig. 2d-e) the fluctuation amplitude increases to $\tilde{n}/n \approx 0.3$, which strongly influences the density profile. The mode pattern becomes irregular but a dominance of the $m = 1$ drift mode is clearly observed, which indicates an energy transfer towards the larger scales in the nonlinear state, as expected from the dual cascade mechanism. In the plasma edge several isolated turbulent structures are observed, that are not connected to the drift-wave dynamics and lead to the observed broadening of the density profile in Fig. 2d.

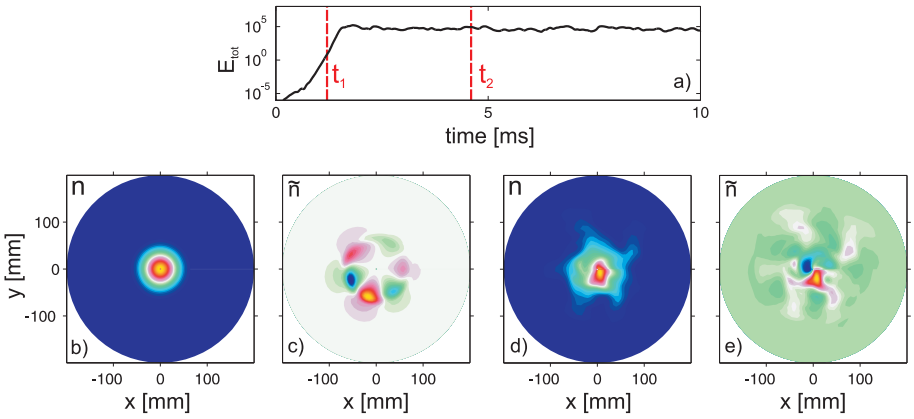

Figure 2. Temporal evolution of the total fluctuation energy E_{tot} (a) and snapshots of n and $\tilde{n}$ in the linear (b,c) and nonlinearly saturated phase (d,e) at the axial center of the simulation domain in a plane perpendicular to the background magnetic field. The time instants are indicated in a) as red lines.

2.3. Plasma parameter profiles

Measured time-averaged profiles of plasma density and plasma potential are shown in Fig. 3a. The plasma density is almost a Gaussian with a peak density of $n \approx 6 \cdot 10^{18}\,\mathrm{m}^{-3}$ and a $1/e$-folding length of 40 mm. The plasma potential profile is also peaked in the center but much broader than the density profile ($1/e$-folding length of 150 mm). In the plasma center the electron temperature (not shown) is 2.5 eV and

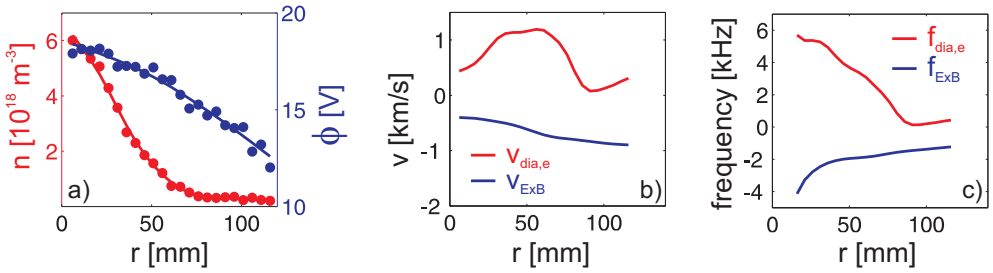

Figure 3. Measured radial profiles of time-averaged plasma density and potential (a), fluid drift velocities (b) and fluid drift frequencies (c).

decreases to 1 eV for larger radii ($r \approx 100\,\mathrm{mm}$). From the profiles shown in Fig. 3a the first order fluid drifts, i.e. the electron diamagnetic drift $v_{dia,e} \sim -\nabla \ln n/B$ and the $E \times B$-drift $v_{E\times B} = E_\perp \times B/B^2$, can be derived. The result is found in Fig. 3b. The electron diamagnetic drift peaks at the maximum density gradient at $v_{dia,e} = 1\,\mathrm{km/s}$ and dominates the total drift velocity $v_{tot} = v_{dia,e} + v_{E\times B}$ for $r \leq 70\,\mathrm{mm}$. Note that, due to the radial run of the time-averaged profiles, the two drift velocities have opposite sign. The modulus of the $v_{E\times B}$-velocity increases almost linearly from the plasma center ($v_{E\times B} = -500\,\mathrm{m/s}$) to the plasma edge ($v_{E\times B} \approx -1000\,\mathrm{m/s}$ at $r = 100\,\mathrm{mm}$). The corresponding drift frequencies $f = v/(2\pi r)$ are shown in Fig. 3c.

The time-averaged radial profiles of the simulated plasma density and potential are shown in Fig. 4a. Compared to the Gaussian density profile in the linear phase, a significant broadening for $r \geq 40\,\mathrm{mm}$ is observed for the nonlinear phase. In agreement to the experimental observation, the self-consistent potential profile is peaked in the plasma center; it has however a much smaller peak amplitude $\phi_{r=0} \approx 0.8\,\mathrm{V}$. The radial variation of the plasma potential profile is much smaller than in experiment, which leads to a smaller background $E \times B$-drift, as shown in Fig. 4b. Across the entire profile the electron diamagnetic drift $v_{dia,e}$ is dominant.

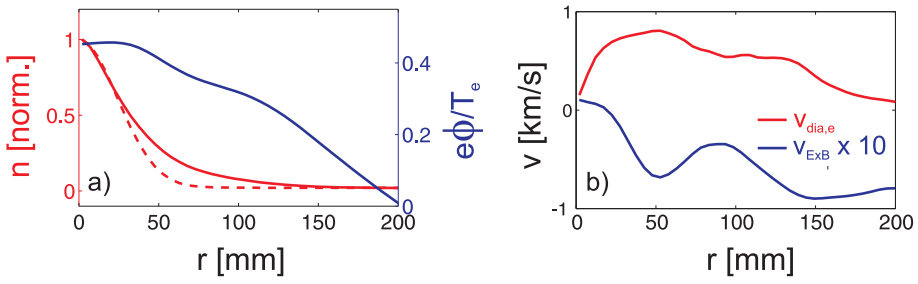

Figure 4. Radial profiles of simulated plasma density and potential in the nonlinearly saturated state (a, solid lines). For comparison the density profile in the linear phase is also shown as dashed line. The corresponding first order fluid drifts are shown in b).

3. Intermittent transport events

The typical character of the plasma density fluctuations in the edge plasma is summarized in Fig. 5a (experimental). The time series have been recorded at a distance 80 mm from the plasma center (cf. Fig. 3a). One finds sporadic density bursts with large amplitudes of $n_{burst} \approx 4 - 5\sigma$ (σ denotes the standard deviation), which leads to a highly non-Gaussian probability distribution function (PDF) with long positive tails. The corresponding moments of the PDF, skewness S and kurtosis K, are $S = 1.3$ and $K = 1.6$. In the far plasma edge ($r \approx 120$ mm) these values increase to $S = 3.5$ and $K = 15$. Using a wavelet analysis it can be demonstrated that the kurtosis increases monotonically with the frequency (not shown). Hence, the density fluctuations can be considered as intermittent in the strict sense [10]. At the same time the potential fluctuations (Fig. 5b) exhibit a more Gaussian character with $S = -0.5$ and $K = 0.8$. The spectra of density and potential fluctuations (Fig. 5c) have quite a similar shape. In both cases, a bump at a frequency of ≈ 1.2 kHz indicates the typical temporal occurrence of the density bursts. For larger frequencies the spectra show a power-law decay $f^{-\alpha}$ with a spectral index $\alpha = 4.3$.

For comparison with the experiment, the time series and frequency spectra of the simulated data are shown (same representation) in Fig. 5d-f. The data has been obtained at $r = 130$ mm. Intermittent large-amplitude density bursts of $6\,\sigma$ are observed as well, but the PDF has a more Gaussian character with $S = 1.8$ and $K = 5.7$. The density bursts can be seen in the spectrum in Fig. 5f as a bump at 350 Hz, which is less than in the experimental situation. The decrease of the fluctuation energy for $f > 10$ kHz is much steeper than in experiment. This is most likely caused by overemphasized viscous damping factors in the numerical simulation. At the same position the potential fluctuations (Fig. 5e) are Gaussian with smaller fluctuation amplitudes ($\approx 2\,\sigma$). This agrees with the experimental case.

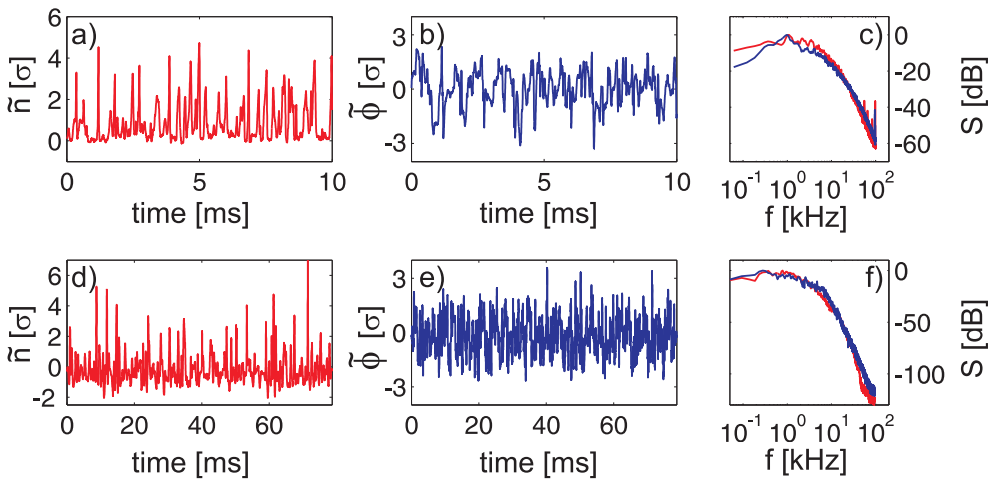

Figure 5. Measured normalized time series of density and potential fluctuations in the plasma edge for the experimental (a,b) and simulated (d,e) data. The corresponding frequency spectra are shown in c) and f), respectively.

4. Propagation of coherent turbulent structures in the plasma edge

To investigate the origin of the large-amplitude density bursts, a spatiotemporal analysis using the conditional averaging (CA) technique [29, 30] is applied. It is based on the statistical comparison of two simultaneously recorded time series at different spatial positions: One time series is recorded at a a fixed spatial position $\mathbf{r_0}$ and acts as a reference signal $R(\mathbf{r}_0, t)$. The other time series is recorded simultaneously, but at a different spatial position $\mathbf{r}_0 + \mathrm{d}\mathbf{r}$ and is called the displaced signal $D(\mathbf{r}_0 + \mathrm{d}\mathbf{r}, t)$. When the reference signal R fulfills a pre-defined condition p at a certain time instant t_i, a time interval of length $\Delta\tau$ centered around t_i is extracted from both time series. If the condition is fulfilled N times, the N sub-timeseries are taken as statistically independent realizations. By ensemble averaging of the sub-time series, the coherent part of the fluctuations is extracted while the incoherent part is suppressed. The conditional averaging procedure can be written as

$$\langle R \rangle_{\mathrm{CA}} (\mathbf{r}_0 + \mathrm{d}\mathbf{r}, \tau) = \frac{1}{N} \sum_{\mathrm{i}=1}^{N} \mathrm{D_i}(\mathbf{r}_0 + \mathrm{d}\mathbf{r}, \mathrm{t_i} + \tau), \quad \tau \in [-\Delta\tau/2, \Delta\tau/2] \,. \quad (1)$$

The condition p is a free parameter and is chosen here as a threshold condition on the amplitude combined with a slope condition. Events that reach the predefined threshold amplitude within an amplitude interval of $p \pm 5\%$ are detected at falling slope. The time interval is chosen to be $\Delta\tau = \pm 100\mu$s. The resulting conditionally averaged density fluctuations for the experimental situation in a plane perpendicular to the background magnetic field are shown in Fig. 6 for four different time instants. The fixed reference probe is located a $x = -100\,$mm and $y = 0$ (indicated by a black dot). In order to extract the fluctuations that are associated with the large-amplitude density bursts, the amplitude condition was set to $p = 3\sigma$. One observes a propagating structure. Since its lifetime exceeds the eddy turnover time the structure can be considered as coherent structure [33]. The coherent structure propagates mainly azimuthally counter-clockwise in the direction of the background $E \times B$-drift (cf. Fig.3a) but has also a certain radial velocity component directed radially outwards.

The azimuthal and radial velocities can be determined by tracking the experimentally observed structure in the time domain. The evolution of the azimuthal

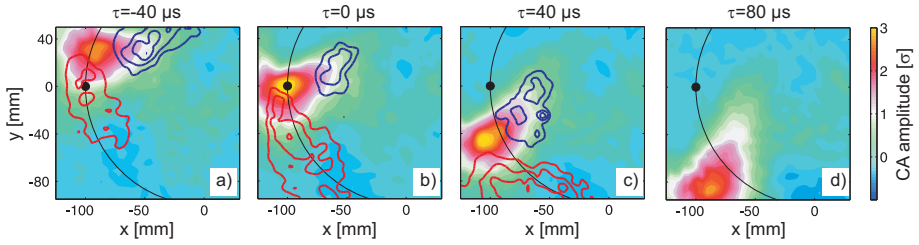

Figure 6. Four time instants of the conditionally averaged density fluctuations as observed in experiment. They are in a plane perpendicular to the background magnetic field, which points into the plane. The position of the reference probe is indicated by a black dot. Superimposed as contour lines are positive (red) and negative (blue) potential fluctuations associated with the coherent structure. The solid black line indicates a purely azimuthal propagation.

and radial position of the structure is shown in Fig.7a for $\tau = -62 \ldots 58\,\mu$s. The resulting azimuthal and radial velocities are $v_\theta = 932\,$m/s and $v_r = 213\,$m/s, respectively. In normalized units, the radial velocity corresponds to approximately 10% of the local ion sound speed. The azimuthal velocity corresponds to a frequency $f = v/2\pi r = 1.4\,$kHz. Hence, each density burst in the timeseries of Fig.5a is related to a propagating coherent structure. Inspecting the drift velocities shown in Fig.3b lead to the conclusion that the azimuthal propagation of the structure is solely determined by the background $E \times B$-drift, which has a value of 950 m/s at the radial position of the reference probe. In contrast, the radial velocity component is determined by the self-consistent potential fluctuations that are related to the structure. They are imposed in Fig. 6 as contour lines. Each density structure is associated with a dipolar potential perturbation with the positive potential perturbation being ahead of the density structure. This has also been observed in the LAPD device [20]. The potential dipole causes an azimuthal electric field that gives rise to a radial $E \times B$-velocity $\tilde{v}_r$ which propels the structure radially outwards. By applying in Fig. 6 an azimuthal cut through the density structure at a certain time instant, the resulting self-consistent $\tilde{v}_r$-velocity can be easily computed. The resulting evolution of the density, potential and $\tilde{v}_r$ along the azimuthal trajectory are shown in Fig. 7b for the time instant $\tau = -10\,\mu$s. Since density and potential fluctuations are phase shifted the maximum of $\tilde{v}_r$ agrees with the peak of the density structure and its magnitude is in good agreement with results obtained from tracking the structure (indicated in Fig. 7b by the dashed line). Hence the radial propagation is a self-consistent feature of the coherent structure. To investigate the origin of the dipolar potential structures in more detail, their parallel wavelength has been measured. A radial profile of the dominant frequency component and the related parallel wavelength are shown in Fig. 7c. The wavelength has been measured with two Langmuir probes separated along the magnetic field by a distance

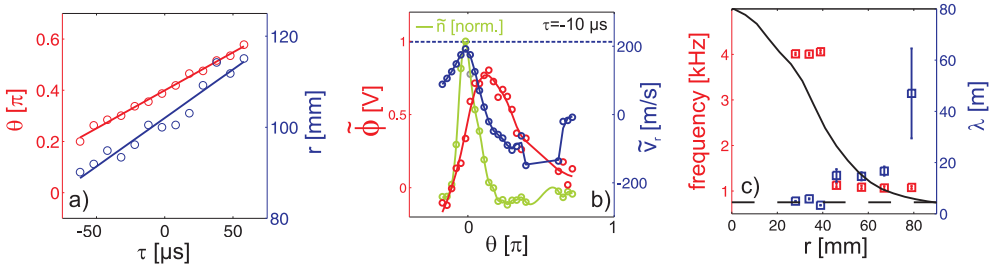

Figure 7. a) Temporal evolution of the azimuthal (red) and radial (blue) position of the coherent structure in Fig. 6. b) Azimuthal cut through the density structure at a time instant $\tau = -10\,\mu$s. Shown are the normalized density (green) and absolute potential (red) fluctuations, as wells as the resulting radial $E \times B$-drift $\tilde{v}_r$ (blue). The dashed line indicates the radial velocity obtained from tracking the structure ($v_r = 213\,$m/s). c) Radial profile of the parallel wavelength (blue) estimated at the main frequency component (red) of the cross-power spectrum between two axially separated probes. The dashed line indicates the machine length $L_\parallel$ and the solid black line indicates the density profile

of $\Delta z = 2\,\mathrm{m}$. For a careful alignment an emissive probe has been attached to one of the probe pins. From the cross-power spectrum of the two probe signals, the wavelength is estimated as $\lambda = 2\pi\Delta z/\delta$, where δ is the phase shift at the main frequency component. In the plasma edge region ($r > 50\,\mathrm{mm}$) the peak in the cross-power spectrum occurs at approximately 1.2 kHz which agrees with the azimuthal propagation of the coherent structures discussed above. In this region the parallel wavelength clearly exceeds the machine length by far ($\lambda \approx 45\,\mathrm{m}$ at $r = 80\,\mathrm{mm}$), which indicates a flute-like character of the fluctuations. The decrease of the wavelength at $r > 50\,\mathrm{mm}$ which is accompanied by an increase of the frequency is discussed in the next section.

The occurrence of isolated turbulent structures in the plasma edge region can be observed in the numerical simulation data (Fig. 2d). The investigation of single events is not very revealing if the close comparison to the experiment is desired. Therefore we apply the conditional averaging technique to the numerical simulation data as well. The reference probe is located in the plasma edge at $r = 123\,\mathrm{mm}$ and the amplitude condition was set to $p = 2\,\sigma$ to reconstruct the dynamics of the large amplitude bursts (cf. Fig.5c). The resulting conditionally averaged density fluctuations in a plane perpendicular to the magnetic field are shown in Fig. 8 for four time instants. The position of the reference probe is indicated by a black dot. Similar to the experiment one observes a coherent structure which propagates mainly azimuthally in direction of the background $E \times B$-drift (cf. also Fig. 6). It also has a certain radial outwards directed velocity component. The velocity components are found from tracking the structure (Fig. 9a). The azimuthal and radial velocities are $v_\theta = 142\,\mathrm{m/s}$ and $v_r = 89\,\mathrm{m/s}$, respectively. The azimuthal velocity is about a factor of two larger than the typical background $E \times B$-drift at the radial position where the structure exists ($v_{E\times B} \approx 80\,\mathrm{m/s}$). The radial structure velocity is solely determined by the self-consistent potential perturbation. They are imposed in Fig. 6 as contour lines. The structure is associated with a dipolar potential perturbation and the resulting $E \times B$-drift propels the structure radially outwards.

Applying the same analysis as done for the experimental data (cf. Fig. 7b), the self-consistent radial velocity $\tilde{v}_r$ can be computed. The result along the azimuthal trajectory of the structure is depicted in Fig. 9b. Shown are the phase-shifted

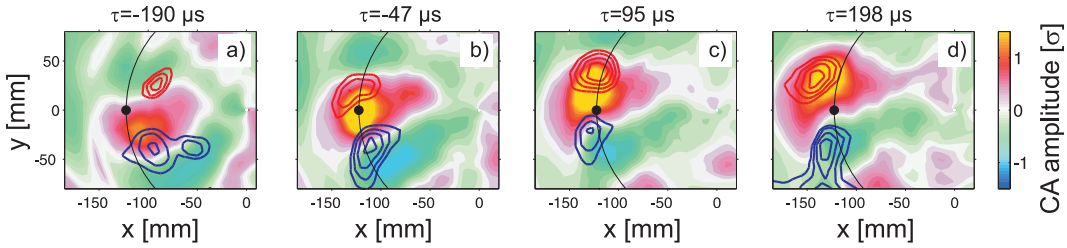

Figure 8. Four time instants of the conditionally averaged density fluctuations of the simulated data (color-coded) in a plane perpendicular to the background magnetic field, which points out of the plane. The position of the reference probe is indicated by a black dot. Superimposed as contour lines are positive (red) and negative (blue) potential fluctuations associated with the coherent structure. The solid black line indicates a purely azimuthal propagation.

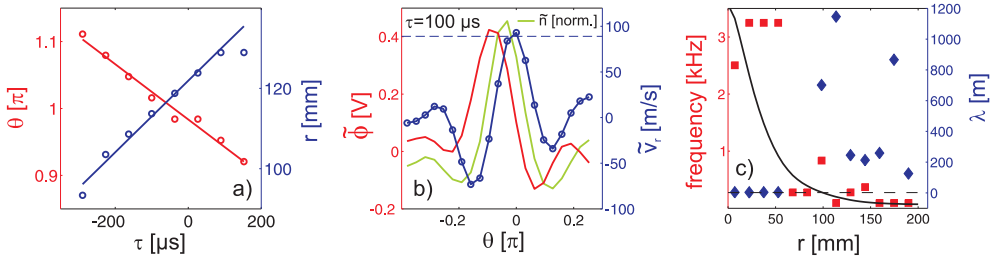

Figure 9. a) Temporal evolution of the azimuthal (red) and radial (blue) position of the coherent structure observed in Fig. 8. b) Azimuthal cut through the density structure at a time instant $\tau = 100\,\mu$s. Shown are the normalized density (green) and absolute potential (red) fluctuations, and the resulting radial $E \times B$-drift $\tilde{v}_r$ (blue). The dashed line indicates the radial velocity obtained from tracking the structure ($v_r = 89\,$m/s). c) Radial profile of the parallel wavelength (blue) estimated at the main frequency component (red) of the cross-power spectrum between two axially separated probes. The dashed line indicates the machine length $L_\parallel$ and the solid black line indicates the density profile.

normalized density and potential perturbation, related to the structure for one time instant, and the estimated $\tilde{v}_r$-velocity. In the region where the density peaks $\tilde{v}_r$ agree well with the result found from tracking the structure (indicated in Fig. 9b by the dashed line). The flute-like character of the coherent structures can be seen in Fig. 9c, that shows a radial profile of the parallel wavelength λ. In agreement with the experiment (cf. Fig. 7c), the wavelengths of the coherent structures in the plasma edge exceed by far the machine length $L_\parallel$ (in this case 2-3 orders of magnitude), such that $k_\parallel \approx 0$. In contrast, in the maximum density gradient region ($r < 60\,$mm), $k_\parallel$ is mainly determined by $L_\parallel$ owing to the three-dimensional drift-wave dynamics.

The dipolar potential perturbation of the coherent structure is directly related to two current filaments $\tilde{j}_\parallel$. The experimental observation is shown in Fig. 10a as current contour lines, together with the conditionally averaged density fluctuations (at $\tau = 15\,\mu$s). The same is shown for the simulation data in Fig. 10b (at $\tau = 11\,\mu$s). The magnitude of the current density is typically $20\,\mathrm{mA/cm^2}$ in experiment and $50\,\mathrm{mA/cm^2}$ in the numerical simulation. This value must be compared to the sheath current, which sets an upper limit for the parallel current:

$$\tilde{j}_{\parallel,s} = e\tilde{n}\left(\sqrt{e\frac{T_e+T_i}{m_{Ar}}} - \sqrt{\frac{eT_e}{2\pi m_e}}\exp(-\frac{\tilde{\phi}}{T_e})\right).$$

Inserting the experimental values for the coherent structures in the plasma edge ($n = 2\cdot 10^{18}\,\mathrm{m^{-3}}$, $\phi = 0.8\,$V, $T_e = 0.8\,$eV and $T_i = 0.2\,$eV) one obtains $j_{\parallel,s} = 1.3\,\mathrm{A/cm^2}$, much larger than the measured value. Another approach is to estimate $\tilde{j}_\parallel$ directly from the parallel electric field between the coherent structure and the the grounded end plate. The electric field is $\tilde{E} = 0.15\,$V/m for a typical wavelength $\lambda = 20\,$m (cf. Fig. 7c) and a connection length of 2 m away from the measurement position. The current density is then given by $\tilde{j}_\parallel = \tilde{n}e\mu\tilde{E}$, where $\mu = e/m_e\nu_{ei}$ is the classical electron mobility. For the values used above one obtains $\tilde{j}_\parallel = 12\,\mathrm{mA/cm^2}$, which is in agreement with the experimental observation. A similar analysis for the simulation

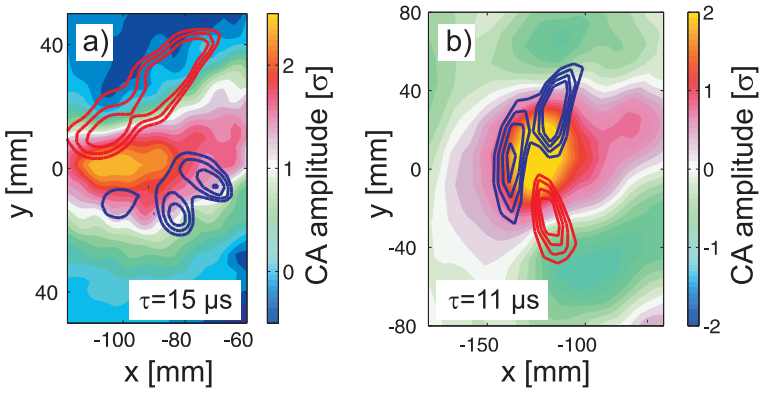

Figure 10. Conditionally averaged density fluctuations (color-coded) and current density $\tilde{j}_{\parallel}$ imposed as contour lines for the experiment (a) and numerical simulation (b).

data yields $\tilde{j}_{\parallel} = 1.6\,\mathrm{mA/cm^2}$, which is much smaller than the observed value. Thus, the parallel current is not limited by the sheath boundary conditions but adjusts in response to the electric field determined by the structure's amplitude and its finite parallel wavelength.

Different mechanisms have been suggested to explain the polarization in linear magnetic field geometry, e.g., centrifugal forces due to a rigid body plasma rotation [34] or the neutral wind due to different heating rates of neutrals in the plasma core and edge regions, which results in a net radial force [22]. Assuming that the polarization of the turbulent structure originates from the neutral wind, we can estimate the resulting radial velocity. Inserting the experimentally observed peak density of the coherent structures and assuming temperatures of $T_0(r=0) = 0.05\,\mathrm{eV}$ and $T_0(r=a) = 0.02\,\mathrm{eV}$ for the neutral argon gas, in the core plasma and in the edge plasma, respectively, we obtain from the neutral wind model a radial structure velocity of $v_{nw} = 172\,\mathrm{km/s}$ for the turbulent structure, which is in good agreement with the experimental findings.

5. Formation of coherent structures

Previous investigations have shown that the drift-wave mechanism is the dominant instability in the VINETA device [35, 36]. It is driven by the radial pressure gradient which provides the free energy. The non-adiabatic parallel electron dynamics leads to a three-dimensional structure of the drift-wave with $k_{\parallel} > 0$. Due to the cylindrical boundary conditions drift waves exhibit a mode structure with an azimuthal modenumber $m = k_{\perp}/r$. The propagation is in the direction of the electron diamagnetic drift. Depending on the background magnetic field, single coherent modes with $m \leq 12$ or weakly-developed drift-wave turbulence are observed. The transition to turbulence is governed by an increase of the nonlinear coupling between various drift modes [37] and an energy transfer towards the larger scales, as expected from the dual cascade [11]. A typical radial spectrogram of density fluctuations in the weakly developed turbulent regime is shown in Fig. 11a. The spectrum separates into two distinct regions: For $x < 50\,\mathrm{mm}$, the energy of the fluctuations is concentrated at a frequency of $\approx 4\,\mathrm{kHz}$. At $x \approx -50\,\mathrm{mm}$ a sudden transition to $f \approx 1\,\mathrm{kHz}$ is observed.

The frequency-wavenumber (k, f)- spectrum at this position (Fig. 11b) shows two counter-propagating phase velocity branches at the same radial position. The branch for negative modenumbers is directed in parallel to the electron diamagnetic drift and the branch with positive modenumbers in direction of the background $E \times B$-velocity. From the (k, f)-spectrum we find that the peak at $\approx 4\,\mathrm{kHz}$, observed in Fig. 11a, is related to a $m = 1$ drift mode propagating in electron diamagnetic drift direction. The measured frequency of the $m = 1$ drift mode can be compared to the Doppler-shifted Hasegawa-Mima dispersion relation

$$\omega = \omega_{dia,e}/(1 + (k_\perp \rho_s)^2)) + k_\perp E_\perp / B.$$

Taking the time-averaged profiles Fig. 3a, the dispersion relation yields a frequency of $f = 3.9\,\mathrm{kHz}$ for the $m = 1$ drift mode at $r = 36\,\mathrm{mm}$, which is in good agreement with the experimental finding. The measured parallel wavelength $\lambda_\parallel$ of the $m = 1$ drift mode has already been shown in Fig. 7c. In the region where the drift mode exists ($r \leq 40\,\mathrm{mm}$), $k_\parallel$ is determined by the machine length $L_\parallel$.

The branch of the phase velocity in $E \times B$-drift direction in Fig. 11c is also dominated by an $m = 1$ structure with a frequency of $f \approx 1.3\,\mathrm{kHz}$, which is in agreement with the background $E \times B$-frequency as shown in Fig. 3c at $r = 50\,\mathrm{mm}$. The temporal evolution of the modenumber spectrum at $r = 50\,\mathrm{mm}$ is shown in Fig. 11c. As expected from the (k, f)-spectrum the energy is concentrated at modenumber $m = 1$, but higher modenumbers are observed as well. This happens

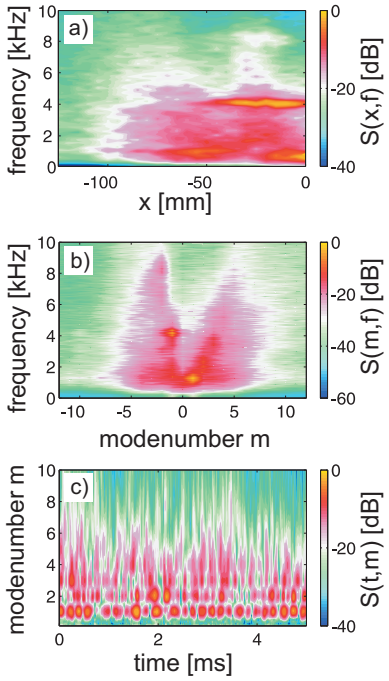

Figure 11. Doppler-shifted radial spectrogram of density fluctuations (a) and frequency-wavenumber spectrum measured at $r = 50\,\mathrm{mm}$ (b). The temporal evolution of the wavenumber spectrum at $r = 50\,\mathrm{mm}$ is shown in (c).

especially if the quasi-coherent $m = 1$ mode breaks down, which indicates an energy transfer towards smaller scales.

The (k, f)-spectrum of the simulated data is shown in Fig. 12b. It has been recorded at $r = 35\,\mathrm{mm}$. Similar to the experimental situation negative modenumbers correspond to a propagation in electron diamagnetic drift direction and positive modenumbers in direction of the background $E \times B$-drift (cf. also Fig. 11a). Two azimuthally counterrotating branches of the phase velocity are observed and the dominant $m = 1$ drift mode has a frequency of $f \approx 500\,\mathrm{Hz}$. As already mentioned, this deviates significantly from the typical electron diamagnetic drift frequency as estimated from the time-averaged profiles at this radial position. This deviation can be understood if we consider in addition the (k, f)-spectrum at $z = 0$ (Fig. 12a). Here, the frequencies of the dominant drift modes $m = 1, 2$, $f_{m=1} = 2.7\,\mathrm{kHz}$ and $f_{m=2} = 3.2\,\mathrm{kHz}$, respectively, are in agreement with the dispersion relation. The nonlinear coupling between these modes is described by three-wave interaction obeying the summation rule for the modenumber $m_3 = m_1 \pm m_2$ and frequency $f_3 = f_1 \pm f_2$. As a result of the nonlinear interaction, a $m = 1$ drift mode occurs at $f = 500\,\mathrm{Hz}$. The bicoherence, which is a measure for the phase coupling due to this three-wave interaction, is $b^2 = 0.28$, much larger than the noise limit. The reason why this beating mode becomes dominant at larger distances to the source region ($z \gg 0$) is not yet fully understood. The temporal evolution of the modenumber spectrum (Fig. 12c) underlines the dominance of the quasi-coherent $m = 1$ drift mode, but it also shows strong contributions of fluctuations with smaller scales if the energy of the $m = 1$

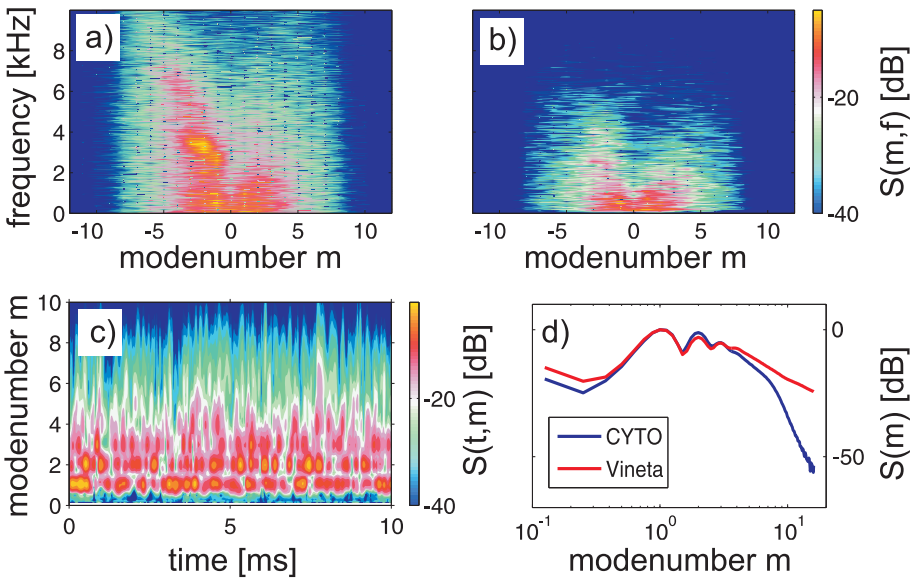

Figure 12. Frequency-wavenumber spectra of density fluctuations obtained at $r = 35\,\mathrm{mm}$ and $z = 0$ (a) and $z = L/2$ (b). Temporal evolution of the modenumber spectrum at $r = 35\,\mathrm{mm}$ and $z = L_\parallel/2$ (c). Time-averaged modenumber spectra of the experimental situation (VINETA) and numerical simulation (CYTO) (d).

.

mode is reduced. A comparison of the time-averaged modenumber spectra between the experimental and numerical simulation is shown in Fig. 12d. Good agreement is found for the large scale fluctuations, which carry the main energy. For $m > 7$ a strong deviation is seen, which has been observed already in the frequency spectra (cf. Fig. 5c,f)

In order to investigate the transition region of the radial spectrogram at $r \approx 50\,\mathrm{mm}$ in more detail, the spatiotemporal dynamics has been reconstructed using the CA technique in a similar way as in Sec. 2.2. The resulting conditionally averaged density fluctuations in a plane perpendicular to the magnetic field are shown in Fig.13 for four different time lags τ. The reference probe is located at $x = 40\,\mathrm{mm}$ and $y = 0$ and the amplitude condition was set to σ. For the consecutive time lags one clearly observes a $m = 1$ drift mode propagating clockwise in the direction of the electron diamagnetic drift. The amplitude of the drift mode is not constant for the different time lags. While for $\tau \leq 40\,\mu\mathrm{s}$ the $m = 1$ drift mode dominates, the fluctuation amplitude is strongly reduced at $\tau = 60\,\mu\mathrm{s}$ and the mode pattern becomes more irregular. This quasi-coherent behavior has also been observed in Fig. 11c.

During propagation, the $m = 1$ mode is subject to a sheared azimuthal velocity, which leads to an azimuthal elongation of the positive density perturbation for $\tau = 0 \ldots 40\,\mu\mathrm{s}$ at $x = -50\,\mathrm{mm}$. This elongation goes along with a radial displacement towards the plasma edge. Since the $m = 1$ drift mode continues to propagate clockwise and the elongated structure starts to propagate counter-clockwise in the direction of the background $E \times B$-drift, both get finally disconnected at $\tau = 60\,\mu\mathrm{s}$ and an isolated coherent structure develops. This peel-off process might cause the break down of the $m = 1$ drift mode. The sheared azimuthal propagation cannot be explained by the radial profiles of the fluid drifts (Fig. 3b). At $x = -50\,\mathrm{mm}$ the electron diamagnetic drift velocity is a factor of two larger than the background $E \times B$-drift. The peel-off process is rather caused by the self-consistent potential fluctuations associated with the $m = 1$ drift mode. They are shown in Fig.13 as contour lines. At $\tau = -30\,\mu\mathrm{s}$ the azimuthal phase shift $\delta_{\tilde{n},\tilde{\phi}}$ between density and potential fluctuations is approximately $\pi/3$ and the resulting fluctuation induced transport $\Gamma = \tilde{n}\tilde{v} \sim k_\theta\, \tilde{n}\tilde{\phi}\, \sin \delta_{\tilde{n},\tilde{\phi}}$ transports plasma particles radially outwards. Since density and potential perturbations also exhibit a radial displacement plasma particles are also transported azimuthally away

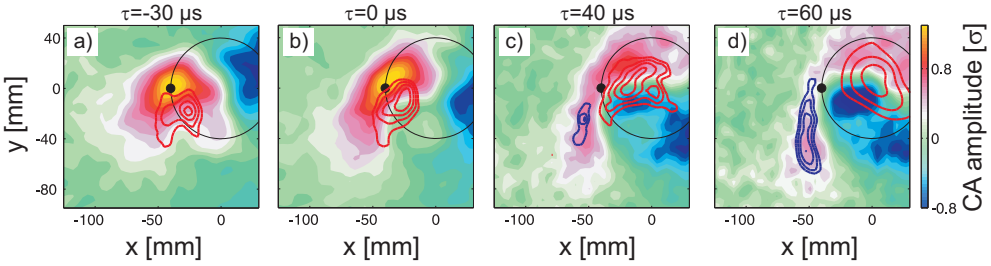

Figure 13. Four time instants of the conditionally averaged density fluctuations of the experimental situation (color-coded) in a plane perpendicular to the background magnetic field, pointing into the plane. The position of the reference probe is indicated by a black dot. Superimposed as contour lines are positive (red) and negative (blue) potential fluctuations.

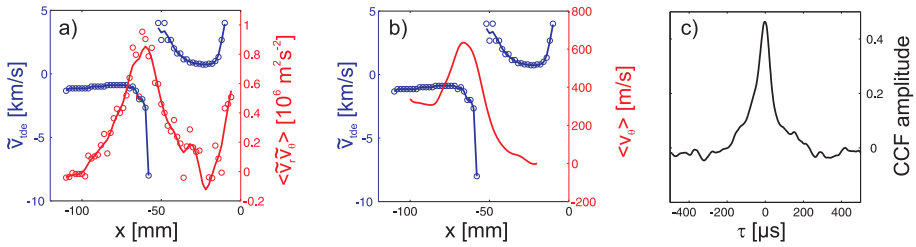

Figure 14. Radial profiles of the phase velocity $\tilde{v}_{tde}$ (blue) and turbulent Reynolds stress (red, taken here as time average) (a) of the experimental situation. The time-averaged azimuthal velocity $< v_\theta >$ as estimated from the ion-momentum equation [2] (b, red line). The cross-correlation amplitude between the azimuthally averaged Reynolds stress and the spectral energy of the $m = 0$ mode (c).

from the drift mode, which leads to the observed azimuthal elongation. A careful analysis of Fig. 13d reveals that the disconnected structure is directly related to a negative potential perturbation. This might be explained by a local increase of the electron temperature due to energy transport, which would cause a decrease of the floating potential.

To investigate the observed azimuthal velocity shear of the fluctuations, the time-delay method has been utilized [38]. Fluctuations are measured at different radial positions with two azimuthal separated probes. The time-lag of the maximum of the cross-correlation amplitude between these two signals then yields the average phase velocity $\tilde{v}_{tde}$. The result is shown in Fig. 14a as blue lines. Positive velocities correspond to a propagation in electron diamagnetic drift direction and negative velocities to a propagation in direction of the background $E\times B$-drift. For $x > -40\,\mathrm{mm}$ $\tilde{v}_{tde}$ agrees well with the fluid drifts. In the region $x = -50 \ldots -40\,\mathrm{mm}$ $\tilde{v}_{tde}$ increases to 4 km/s, which deviates significantly from the fluid drifts (Fig. 3b). The transition to the $E \times B$-drift is characterized by a strong shear ($\partial_r \tilde{v}_{tde}$) and occurs at $x \approx -55\,\mathrm{mm}$. While in this region $\tilde{v}_{tde}$ exceeds the time-averaged $E \times B$-velocity by about a factor of 10, good agreement is found in the plasma edge region $x < -70\,\mathrm{mm}$. The formation of this radially localized azimuthal shear layer can possibly be explained by considering the electrostatic turbulent Reynolds stress

$$R = \langle \tilde{v}_r \tilde{v}_\theta \rangle_\theta = -\left\langle \tilde{E}_r \tilde{E}_\theta \right\rangle_\theta / B_0^2,$$

which is a measure for the anisotropy of the $E \times B$-velocity fluctuations. $\langle\cdot\rangle_\theta$ denotes the azimuthal average. To estimate the radial evolution of the Reynolds stress, the azimuthal average $\langle\cdot\rangle$ is taken as time average $\langle\cdot\rangle_t$ and the fluctuating radial and azimuthal electric fields are estimated by the difference between floating potential fluctuations measured with two radially and two azimuthally separated probe tips. Utilizing the azimuthal probe array, the azimuthally averaged Reynolds stress can be measured only at a fixed radial position. The radial evolution of the Reynolds stress is shown in Fig. 14a as red line. In the region where the shear layer exists, an increase of the Reynolds stress is observed. The time-averaged azimuthal component of the ion momentum equation is given by [39]

$$\frac{1}{r^2}\frac{\partial}{\partial r}\left(r^2 < \tilde{v}_r \tilde{v}_\theta >\right) = -\nu_{in} < v_\theta > + \mu_{ii}\frac{\partial^2 < v_\theta >}{\partial r^2} + \frac{1}{r}\frac{\partial < v_\theta >}{\partial r} - \frac{< v_\theta >}{r^2}, \quad (2)$$

where ν_{in} denotes the ion-neutral collision frequency and $\mu_{ii} = 3/10\rho_i^2\nu_{ii}$ denotes the ion viscosity (with ρ_i being the ion gyro radius and ν_{ii} being the ion-ion collision frequency). Since the lhs of equation (2) is known, it can be solved for the time-averaged azimuthal velocity $< v_\theta >$ with the assumption that ν_{in} is constant across the plasma cross section. The result is shown in Fig. 14b. The radial variation of the Reynolds stress leads to an increase of $< v_\theta > \approx 600\,\mathrm{m/s}$ in the shear region, which is much less than the observed variation of the phase velocity here. Taking into account the azimuthally averaged Reynolds stress at $r = 50\,\mathrm{mm}$, a relatively high correlation amplitude of 0.45 between R and the spectral energy of the $m = 0$ mode is observed (Fig. 14c), which clearly demonstrates that the formation of large-scale flows with $m = 0$ are driven by the turbulent Reynolds stress.

The CA analysis has been performed for the numerical simulation data. The conditionally averaged density fluctuations are shown for four time instants in Fig. 15. The reference probe is located in the maximum density gradient and the amplitude condition was chosen to $p = 2\,\sigma$. Due to limited number of samples, the result is not as clear as in experiment (cf. Fig.13) but the peel-off of a turbulent structure from a $m = 1$ drift mode can be observed as well. A $m = 1$ mode is observed that propagates counterclockwise, i.e. in direction of the electron diamagnetic drift. At $\tau = 75\,\mu\mathrm{s}$ a fraction of the positive density perturbation peels radially off of the drift mode and gets disconnected for larger time lags. The isolated turbulent structure propagates azimuthally clockwise in direction of the background $E \times B$-drift. As in experiment, the peel-off can be explained by the relatively large phase shift between density and potential fluctuations, which gives rise to a radial, fluctuation-induced transport. The potential perturbations associated with the density potential perturbation are imposed in Fig. 15 a as red contour lines.

As described before, also in the simulation the peel-off process is associated with a shear of the azimuthal phase velocity of the fluctuations. A radial profile of the average phase velocity $\tilde{v}_{tde}$ is shown in Fig. 16a. Positive velocities correspond to

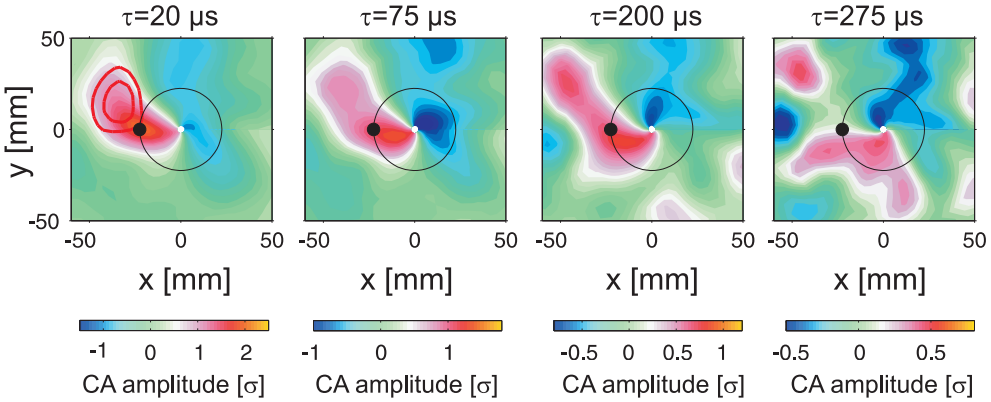

Figure 15. Four time instants of the conditionally averaged density fluctuations of the simulated data (color-coded) in a plane perpendicular to the magnetic field, which points out of the plane. Positive potential perturbations are imposed in (a) as red contour lines. The position of the reference probe is indicated by a black dot.

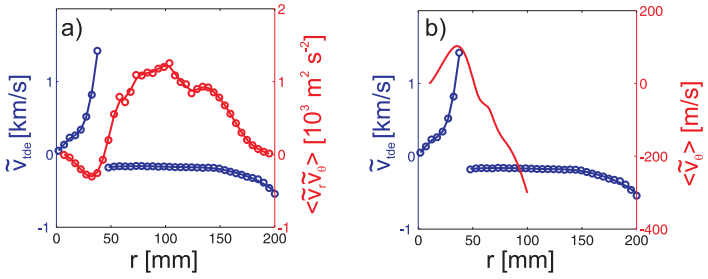

Figure 16. Radial profile of the azimuthal phase velocity v_{tde} of the simulated data estimated using the time-delay method (blue) and Reynolds stress (red, taken here as time average) (a).The time-averaged azimuthal velocity $< v_\theta >$ as estimated from the ion-momentum equation [2] (b, red).

a propagation in electron diamagnetic drift direction and negative velocities to a propagation in direction of the background $E \times B$-drift. While for $r < 40$mm the phase velocity is in agreement with the fluid drifts (Fig. 4b) it significantly deviates at $r \approx 40$ ($\tilde{v}_{tde} \approx 1.5\,$km/s). At $r \approx 45\,$mm a transition to the background $E \times B$-drift is observed. Similar to experiment, the time-averaged turbulent Reynolds stress has been determined as the momentum source. The radial profile of the Reynolds stress is shown Fig. 16a as red line. In contrast to experiment (Fig.14a) the Reynolds stress peaks at a much larger radius ($r \approx 100\,$mm). This is mainly caused by a difference of the radial profile of the potential fluctuation amplitude. But the most important similarity to the experiment is the fact that the radial variation of the Reynolds stress is peaking in the transition region. With the measured Reynolds stress the ion-momentum equation (2) can be solved for the time-averaged azimuthal velocity $< v_\theta >$. The result is shown in Fig. 16b. In the transition region, the radial variation of the turbulent Reynolds stress leads to an increase of $< v_\theta > \approx 100\,$m/s, which is less than the observed deviation of the phase velocity from the fluid drifts.

6. Summary and conclusion

The interrelationship between intermittent fluctuations and weakly developed drift-wave turbulence in the plasma edge of a linearly magnetized plasma column has been investigated by means of experimental observations and numerical simulations. A comparison between time-averaged plasma parameters and fluctuating quantities shows that the numerical result resembles much the experimental situation. The main difference in the simulation is a lower potential amplitude and an overemphasized damping of the fluctuations at larger wavenumbers. It is demonstrated that the large-amplitude density bursts are related to spatiotemporal coherent turbulent structures, which propagate mainly azimuthally but also radially outwards towards the wall. The experimental and simulation data have shown an excellent agreement concerning the propagation and generation of those turbulent structures. While the azimuthal propagation of turbulent structures is determined by the radial electric field and resulting $E \times B$-drift, their radial propagation is caused by the self-consistent dipolar potential perturbation, which is associated with each density structure. Theory

suggest that the polarization of the flute-like density structures is caused by either neutral wind or centrifugal forces [22]. For the typical experimental conditions, the neutral wind force results in a radial structure velocity that is in good agreement with the observations. In the numerical simulations, however, the neutral wind force is not considered, which indicates that rigid body plasma rotation must be taken into account as well.

The formation of coherent structures is closely linked to transport events caused by the nonlinear drift-wave fluctuations. The fluctuation spectrum in the maximum density gradient region is dominated by a quasi-coherent $m = 1$ drift mode. It propagates in direction of the electron diamagnetic drift with a frequency that agrees well with the Hasegawa-Mima dispersion relation. The formation process of the structures can be explained as a peel-off process of density packages from the $m = 1$ drift mode. This process is driven by a relatively large phase shift between density and potential fluctuations of the $m = 1$ mode ($\delta_{\tilde{n},\tilde{\phi}} \approx \pi/3$). This phase shift gives rise to radial fluctuation-induced transport that propels plasma particles radially away from the drift mode. The peel-off leads to a decreasing fluctuation amplitude of the $m = 1$ mode and thus causes the observed quasi-coherent behavior. Once the structures are disconnected from the drift mode, they propagate azimuthally in opposite direction to the drift mode, i.e. in direction of the background $E \times B$-drift. As a result, a strongly sheared azimuthal phase velocity is observed. Since in the transition region the magnitudes of the electron diamagnetic drift and background $E \times B$-drift are well separated, a sharp edge is observed in the radial spectrogram. Due to the counterrotation of the $m = 1$ drift mode and the turbulent structures, two branches are observed in the frequency-wavenumber spectra in the peel-off region.

An analysis of the sheared azimuthal phase velocity using the time-delay method reveals that its magnitude by far exceeds the estimated first order fluid drifts in the transition region. As a possible momentum source, the turbulent Reynolds stress has been considered, which requires a certain correlation between the radial and azimuthal velocity components of the fluctuations. The observed correlation between these velocity components during the peel-off process leads to a local peaking of Reynolds stress. The position where the Reynolds stress peaks is well correlated with the shear layer of the azimuthal phase velocity. The good correlation between the azimuthally averaged Reynolds stress and the energy of the $m = 0$ mode clearly demonstrates the formation of large-scale flows. A quantitative comparison between the measured phase velocity and the corresponding velocity obtained from the momentum equation [39] shows that the contribution of the Reynolds stress is too small to account for the observed variation of the phase velocity. In order to estimate the influence of the Reynolds stress the complete momentum balance including parallel momentum losses must be taken into account.

References

[1] KOLMOGOROV A 1962 *J. Fluid Mech.* **13** 82–85 ISSN 0022-1120

[2] DOUADY S, COUDER Y and BRACHET M 1991 *Phys. Rev. Lett.* **67** 983–986 ISSN 0031-9007

[3] De Michelis P and Consolini G 2004 *ANNALS OF GEOPHYSICS* **47** 1713–1722 ISSN 1593-5213

[4] Alexandrova O, Carbone V, Veltri P and Sorriso-Valvo L 2007 *PLANETARY AND SPACE SCIENCE* **55** 2224–2227 ISSN 0032-0633 International Meeting on Dynamical Processes in Space Plasmas, ISRAEL, MAY 07-15, 2006

[5] Veltri P 1999 *Plasma Phys. Controlled Fusion* **41** A787–A795 ISSN 0741-3335 25th EPS Conference on Controlled Fusion and Plasma Physics / International Congress on Plasma Physics, PRAGUE, CZECH REPUBLIC, JUN 29-JUL 03, 1998

[6] VANMILLIGEN B, HIDALGO C and SANCHEZ E 1995 *Phys. Rev. Lett.* **74** 395–398 ISSN 0031-9007
[7] Carbone V, Regnoli G, Martines E and Antoni V 2000 *Phys. Plasmas* **7** 445–447 ISSN 1070-664X
[8] BATCHELOR G and TOWNSEND A 1949 *PROCEEDINGS OF THE ROYAL SOCIETY OF LONDON SERIES A-MATHEMATICAL AND PHYSICAL SCIENCES* **199** 238–255
[9] Kolmogorov A N 1941 *Dokl. Akad. Nauk. SSSR* **32** 16–18
[10] Frisch U 1995 *Turbulence: The Legacy of A. N. Kolmogorov* (Cambridge University Press)
[11] Kraichnan R H 1967 *Phys. Fluids* **10** 1417–1423
[12] DIAMOND P and KIM Y 1991 *Phys. Fluids B* **3** 1626–1633 ISSN 0899-8221
[13] Diamond P, Itoh S, Itoh K and Hahm T 2005 *Plasma Phys. Controlled Fusion* **47** R35–R161 ISSN 0741-3335
[14] Terry J L, Zweben S J, Hallatschek K, LaBombard B, Maqueda R J, Bai B, Boswell C J, Greenwald M, Kopon D, Nevins W M, Pitcher C S, Rogers B N, Stotler D P and Xu X Q 2003 *Phys. Plasmas* **10** 1739–1747
[15] Zweben S J, Maqueda R J, Stotler D P, Keese A, Boedo J, Bush C E, Kaye S M, LeBlanc B, Lowrance J L, Mastrocola V J, Maingi R, Nishino N, Renda G, Swain D W, Wilgen J B and the NSTX Team 2004 *Nucl. Fusion* **44** 134–153
[16] Kirk A, Ben Ayed N, Counsell G, Dudson B, Eich T, Herrmann A, Koch B, Martin R, Meakins A, Saarelma S, Scannell R, Tallents S, Walsh M, Wilson H R and MAST Team 2006 *Plasma Phys. Controlled Fusion* **48** B433–B441 ISSN 0741-3335 33rd European-Physical-Society Conference on Plasma Physics, Rome, ITALY, JUN 19-23, 2006
[17] Xu G S, Naulin V, Fundamenski W, Rasmussen J J, Nielsen A H and Wan B N 2010 *Phys. Plasmas* **17** ISSN 1070-664X
[18] Krasheninnikov S I 2001 *Phys. Lett. A* **283** 368–370
[19] Ribeiro T and Scott B 2005 *Plasma Phys. Controlled Fusion* **47** 1657–1679 ISSN 0741-3335
[20] Carter T A 2006 *Phys. Plasmas* **13** 010701
[21] Windisch T, Grulke O and Klinger T 2006 *Phys. Plasmas* **13** 122303 ISSN 1070-664X
[22] Krasheninnikov S I and Smolyakov A I 2003 *Phys. Plasmas* **10** 3020–3021
[23] Franck C M, Grulke O and Klinger T 2002 *Phys. Plasmas* **9** 3254–3258
[24] Naulin V, Windisch T and Grulke O 2008 *Phys. Plasmas* **15** 012307 ISSN 1070-664X
[25] Boswell R W 1984 *Plasma Phys. Controlled Fusion* **26** 1147–1162
[26] Rayner J P, Cheetham A D and French G N 1996 *J. Vac. Sci. Technol. A* **14** 2048–2055
[27] Sudit I D and Chen F F 1994 *Plasma Sources Sci. Technol.* **3** 162–168
[28] Latten A, Klinger T, Piel A and Pierre T 1994 *Rev. Sci. Instrum.* **66** 3254–3262
[29] Adrian R J 1979 *Phys. Fluids* **22** 2065–2070
[30] Huld T, Nielsen A H, Pécseli H L and Rasmussen J J 1991 *Phys. Fluids B* **3** 1609–1625
[31] Rahbarnia K, Ullrich S, Sauer K, Grulke O and Klinger T 2010 *Phys. Plasmas* **17** ISSN 1070-664X
[32] Hasegawa A and Wakatani M 1983 *Phys. Rev. Lett.* **50** 682–686
[33] Terry P W 2000 *Phys. Plasmas* **7** 1653–1661
[34] Chen F F 1966 **9** 965–981 URL `http://link.aip.org/link/?PFL/9/965/1`
[35] Schröder C, Grulke O, Klinger T and Naulin V 2004 *Phys. Plasmas* **11** 4249–4253
[36] Schröder C, Grulke O, Klinger T and Naulin V 2005 *Phys. Plasmas* **12** 042103
[37] Brochard F, Gravier E and Bonhomme G 2006 *PHYSICAL REVIEW E* **73** 036403
[38] Benesty J, Chen J and Huang Y 2004 *IEEE TRANSACTIONS ON SPEECH AND AUDIO PROCESSING* **12** 509–519 ISSN 1063-6676
[39] Tynan G R, Holland C, Yu J H, James A, Nishijima D, Shimada M and Taheri N 2006 *Plasma Phys. Controlled Fusion* **48** S51–S73 ISSN 0741-3335